A Numerical Bayesian-Calibrated Characterization Method for Multiscale Prepreg Preforming Simulations with Tension-Shear Coupling

Weizhao Zhang[1, #], Ramin Bostanabad[1, #], Biao Liang[1], Xuming Su[2], Danielle Zeng[2], Miguel A. Bessa[3], Yanchao Wang[4], Wei Chen[1], Jian Cao[1, *]

1. *Northwestern University, Evanston, IL, USA*
2. *Ford Motor Company, Dearborn, MI, USA*
3. *Delft University of Technology, Delft, Netherlands*
4. *Tongji University, Shanghai, China*

** Corresponding author*

[#]Equal contribution

Abstract

Carbon fiber reinforced plastics (CFRPs) are attracting growing attention in industry because of their enhanced properties. Preforming of thermoset carbon fiber prepregs is one of the most common production techniques of CFRPs. To simulate preforming, several computational methods have been developed. Most of these methods, however, obtain the material properties directly from experiments such as uniaxial tension and bias-extension where the coupling effect between tension and shear is not considered. Neglecting this coupling effect deteriorates the prediction accuracy of simulations. To address this issue, we develop a Bayesian model calibration and material characterization approach in a multiscale finite element preforming simulation framework that utilizes mesoscopic representative volume element (RVE) to account for the tension-shear coupling. A new geometric modeling technique is first proposed to generate the RVE corresponding to the close-packed uncured prepreg. This RVE model is then calibrated with a modular Bayesian approach to estimate the yarn properties, test its potential biases against the experiments, and fit a stress emulator. The predictive capability of this multiscale approach is

further demonstrated by employing the stress emulator in the macroscale preforming simulation which shows that this approach can provide accurate predictions.

Keywords: *Prepreg; Preforming; Bayesian Calibration; Gaussian Processes; Multiscale Simulations*

1 Introduction

Carbon fiber reinforced plastics (CFRPs) are of much interest in the industry nowadays because of their superior properties such as high strength-to-weight ratio, high modulus to weight ratio, good dimensional stability, excellent damage tolerance, and good corrosion and fatigue resistance [1-3]. Utilization of these materials in the aerospace and automotive industries leads to significant weight reduction of equipment systems compared to the conventional metal dominated products; resulting in improved fuel economy and carbon emission [4-6].

To automatically manufacture CFRP parts in large quantities, many processes have been proposed and developed including resin transfer molding (RTM) [7, 8], fiber deposition [9-12], pultrusion [13], and thermoforming [14-16]. The latter process is a proper choice to produce parts for transportation equipment as it can provide a high production rate with relatively complicated surface geometries, good product quality, and low facility cost. In the thermoforming process, the first step is to stack layers of thermoset carbon fiber prepregs (i.e., fabric impregnated by uncured thermoset resin) in an optimized fiber orientation combination. Then, these plane laminates are heated to soften the resin and subsequently formed to the desired 3D shape on a press machine during the preforming step. Finally, the parts are cured to solidify the resin and achieve the designed part shape [17, 18]. In the thermoforming process, most of the fiber re-orientation is introduced in the preforming step which replaces the conventional high-cost and low-rate hand

laying work. Since the mechanical stiffness and strength of the composites are mostly affected by the fiber direction [19], the selection of the preforming parameters such as process temperature and initial fiber orientation is important to the performance of a final part.

To optimize the preforming parameters and produce defect-free parts, numerous tests with different parameter combinations are commonly conducted [20]. However, the consumption of raw material and the long development period increase the cost and time of production; hampering the practicality of thermoforming. To address this issue, several computational models based on the finite element (FE) method have been developed to simulate the preforming process to predict the fiber orientation, geometry, wrinkling behavior on the part, and the forming force [4, 14, 20-23]. For reliable predictions, there is a need for characterizing and employing realistic and accurate material properties in the computational models.

Intra-ply tension and intra-ply shear behaviors are the two important material performances that dominate the behavior of the prepreg sheets. Since shear is the most dominant deformation mode in the composite forming, an international collaborative team have developed the widely accepted bias-extension benchmark test to characterize the intra-ply shear accurately [24]. Uniaxial tension test is also employed by many researchers for intra-ply tension characterization because of its convenience in carrying out the test. These two tests provide reliable results but have some drawbacks. The major one is that they achieve limited loading states. For example, the uniaxial tension test can only introduce pure tension deformation while the bias-extension test can only introduce pure shear deformation. Hence, the coupling between tension and shear cannot be physically characterized and subsequently implemented into the numerical model. Although in most cases this neglection will not affect the prediction of geometry and fiber orientation

significantly due to the fact that the shear modulus of the uncured prepreg is always several orders of magnitude smaller than its tensile modulus, it will introduce errors in the prediction of preforming stress and punch force and hence, reduce the analysis accuracy of defects, such as breakage, pull-out, and separation of the fiber yarns.

Several new test devices such as the biaxial tension apparatus [25] and the picture frame apparatus with tension adjustment [26] have been designed to address the above issue. In practice, however, even these complex devices cannot cover the entire strain states that the prepreg will undergo during preforming due to the complexity of three-dimensional geometry and the resulting nonlinear loading paths. Additionally, these experimental characterization methods are at the macroscale and hence do not provide insightful information on how the mesoscale composite structure and constituents affect mechanical properties of the materials. The cost of raw materials and test time also need to be considered in planning experiments.

In this paper, we develop a new multiscale preforming simulation method based on the prepreg characterization by the mesoscopic representative volume element (RVE) to account for the tension-shear coupling and apply it to the preforming simulation of a 2x2 twill thermoset prepreg. To address the challenge of unknown material parameters at mesoscale, a Bayesian model calibration and validation approach is developed for integrating the calibrated mesoscale stress emulator with macroscale part performance simulations. The flowchart of our approach is illustrated in **Fig. 1**. Our method starts by accurately modeling the mesoscopic RVE in terms of both structure and yarn material (aka constitutive) law. Then, we calibrate our RVE simulator against mesoscopic experiments with a modular Bayesian approach to estimate the mesoscopic yarn properties [27] and build an accurate and inexpensive stress emulator. We note that this

emulator is learned at the mesoscale and acts as the non-orthogonal material constitutive law by replacing the expensive mesoscale RVE simulations at each integration point during the macroscale preforming analysis. The validity and predictive power of our approach is tested by comparing the macroscale simulation and experimental results.

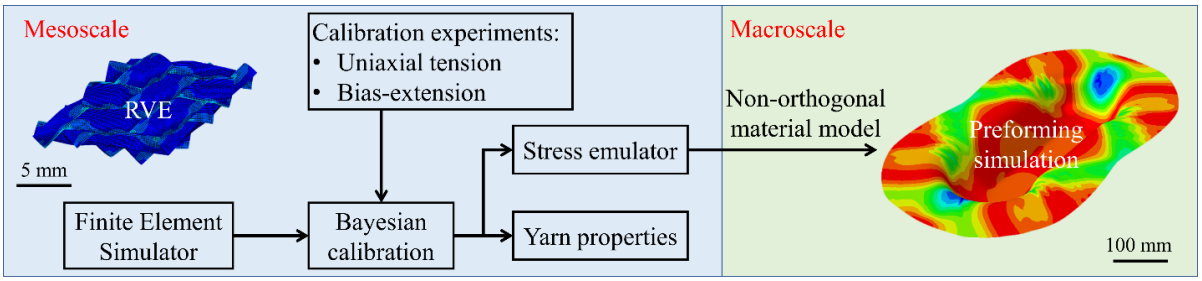

Fig. 1 (Color online) Flowchart of the developed multiscale preforming simulation method: The Bayesian calibration utilizes the RVE and experiments to obtain the yarn properties and the mesoscale stress emulator. The stress emulator is then implemented into the non-orthogonal material model for macroscopic preformation simulation.

The rest of the paper is organized as follows. In Sec. 2, we summarize the experimental measurement of the temperature condition during the preforming process for material characterization. We elaborate on our FE modeling of the mesoscopic RVE (including the structure construction and the yarn material model) in Sec. 3. The developed Bayesian calibration method that identifies the mesoscopic yarn properties and builds the Gaussian process (GP) stress emulator (i.e., mesoscale constitutive law) is detailed in Sec. 4. We validate our approach in Sec. 5 by comparing our macroscale simulation results on the double-dome preforming process against experimental data. The paper is concluded in Sec. 6 by summarizing the contributions and potential future works.

2 Temperature Condition for the Preforming Experiment

Preforming is a temperature varying process because of the hot prepreg sheet and the cold/warm tools used in the process. In our experiment using the double-dome benchmark geometry [28], the

thermoset prepreg was first heated in an oven to around 70 °C and then placed under the press for preforming, see **Fig. 2 (a)**. The press was kept at 23 °C by the coolant within it for fast production rate, so the temperature of the prepreg dropped from the initial value during the process. The temperature history at the top surface center, the bottom surface center, and one side point on the top surface of the prepreg are measured by thermocouples and plotted in **Fig. 2 (b)**.

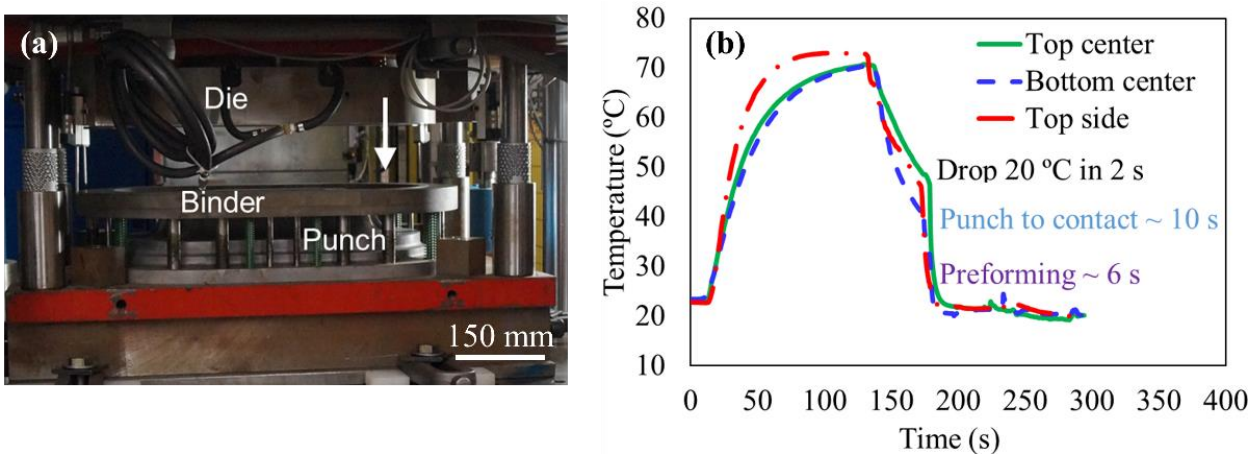

Fig. 2 (Color online) Double-dome preforming test setup: (a) The press for the preforming, and **(b)** the prepreg temperature history plot. The plot indicates that the prepreg temperature drops rapidly from the initial 70 °C to around 23 °C when it is placed under the press.

The plot indicates that the prepreg reached to the temperature of around 70 °C in the oven. Then, it was cooled down gradually to around 45 °C by the air during the transportation from the oven to the press. When it was placed under the press, the cooling rate increased greatly due to the heat conduction between the hot prepreg and the cold metal. In particular, the temperature dropped 20 °C within the first 2 seconds. Meanwhile, it took the press 10 seconds to contact the punch and the prepreg and another 6 seconds to finish the preforming. Therefore, the actual temperature of the prepreg during the preforming process was very close to 23 °C, i.e., the press temperature. As a result, it is reasonable to perform the characterization of the prepreg with uncured thermoset resin and simulate the preforming at the fixed temperature of 23 °C.

3 Mesoscopic RVE Modeling

The RVE is the repeatable unit in the composite material and we model it as dry fabric without the surrounding resin since the prepreg contains soft uncured thermoset resin and its shear stiffness is negligible compared to that of cured composites. Several different approaches have been developed by researchers to construct RVEs with accurate woven patterns and yarn geometrical features because of their significant influence on the RVE stress response under deformation. One approach is to directly use CAD software to design and output the RVE structure [29, 30]. This approach, while being straightforward and suitable for a specific composite structure, is time-consuming because, for each specific composite, the structure needs to be drawn individually, and when the yarn surface geometries become complex, the yarn cross-section shape needs to be manually identified. To generalize the design process and accommodate for more composite structures, geometrical modeling software packages such as TexGen [31] and WiseTex [32] are developed. These packages store large libraries for different composite patterns and can generate the corresponding RVE structure given the geometrical features such as RVE length, yarn width, yarn height, and so on. However, the automatically generated structures usually have fixed shape of the yarn cross-sections and yarn centerlines. These simplifications are suitable for loose woven materials but result in yarn-to-yarn penetration in close-packed composites (see **Fig. 3**). In this case, fine-tuning the geometry by modifying the position, dimension [33], or utilizing non-symmetrical shapes [34] of the local yarn cross-section is essential. These procedures, however, involve complicated geometry manipulation and are time-consuming. For capturing more accurate and detailed structures in RVE, researchers have recently employed X-ray micro-tomography to directly obtain the geometry of the composites [35-37]. This is a promising technique but is quite expensive and requires careful image processing.

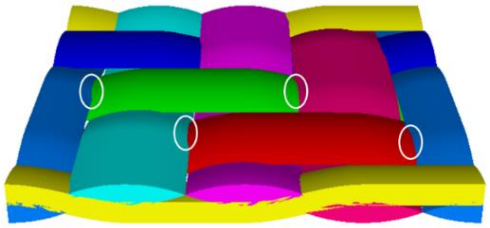

Fig. 3 (Color Online) Yarn-yarn penetration in the RVE: The white circles illustrate locations of the yarn-to-yarn penetration in the composite prepreg RVE geometry model generated by TexGen.

3.1 Construction of the Mesoscopic RVE Structure

To achieve a fine balance between speed and accuracy in generating the RVE structure, we propose a novel 2-step geometrical modeling method with a one-time post-processing to modify the local yarn geometry generated by TexGen. In our method, the rough composite structure without yarn-to-yarn penetration is first generated by TexGen in Step 1 with the specified woven pattern and key characteristic sizes, such as weaving pattern, yarn width, yarn gap, and yarn thickness. Then, the mesh and the local yarn orientation corresponding to the structure is imported to a commercial finite element software, Abaqus Explicit, in Step 2 to compress the structure in the thickness direction to satisfy the prepreg thickness requirements while maintaining the already assigned features. Finally, the deformed mesh and the local material orientation are exported to build the RVE for virtual material characterization.

We employ this method to build a 2x2 twill prepreg with uncured thermoset resin developed by Dow Chemical Company with the surface and cross-section shown in **Fig. 4**. The characteristic dimensions of the yarns and the average thickness of the prepreg are obtained via the Alicona Infinite Focus microscope and the caliper, respectively. The measured data are listed in **Table 1**.

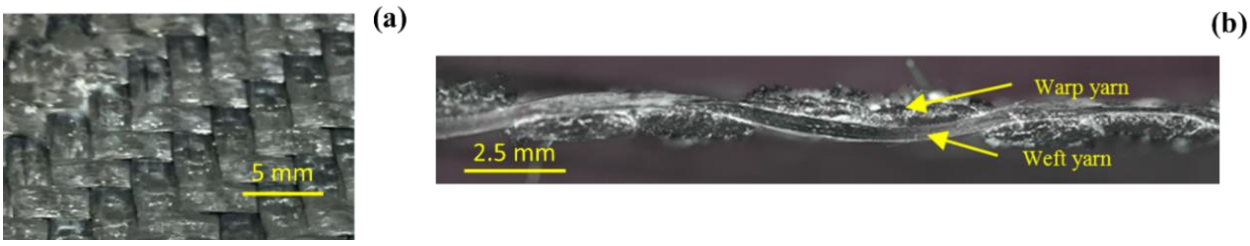

Fig. 4 (Color Online) 2x2 twill prepreg: (a) Surface and **(b)** Cross-section.

Table 1. Characteristic dimensions of the 2x2 twill: The yarn characteristic dimensions (in mm) are obtained via the Alicona Infinite Focus microscope and the average prepreg thickness is measured by the caliper.

Yarn width	Yarn gap	Yarn thickness	Prepreg thickness
2.430 ± 0.112	0.004 ± 0.004	0.503 ± 0.012	0.85 ± 0.15

To construct the RVE structure, we first input the average values of the yarn width, yarn gap, yarn thickness, and the 2x2 twill pattern in TexGen. **Table 1** indicates that the yarn gap is very small, less than 10 μm, compared to the yarn thickness and the yarn width. To minimize the yarn-to-yarn penetration, we set the shape of the yarn's cross-section to lenticular. However, this simple change is insufficient to avoid the penetration completely (see **Fig. 3**), so we artificially enlarge the TexGen prepreg structure thickness from $0.85mm$ to $1.2\ mm$. The result is illustrated in **Fig. 5** and as it can be observed there is no longer any penetration between different yarns.

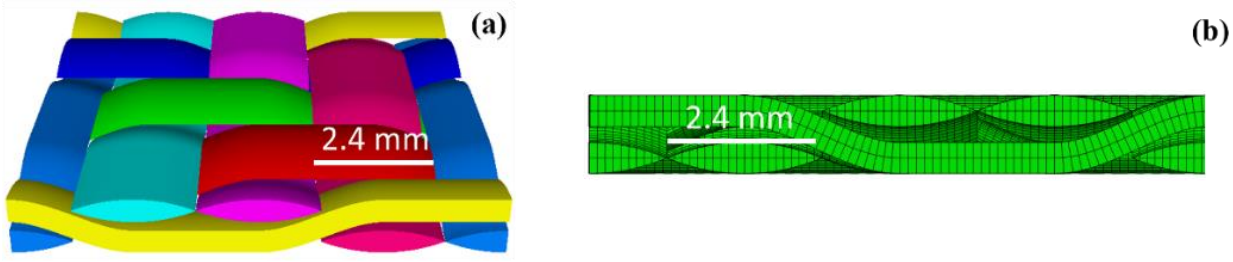

Fig. 5 (Color Online) TexGen rough geometry model with the thickness of the prepreg as of 1.2 mm: (a) The structure, and **(b)** the cross-section of the correspondent mesh.

The drawback of this thickness enlargement, however, is that many gaps are introduced in the structure. Comparison between the cross-section images in **Fig. 4(b)** and **Fig. 5(b)** clearly demonstrates this loose-packed issue. These artificial gaps significantly affect the prediction capability of the RVE simulator: Upon exerting load, the inner gaps will greatly soften the RVE, reduce the response moduli, and elongate the undulation region. To make such a loosely-packed RVE behave similarly to the real prepreg, very large and unrealistic yarn moduli need to be employed for the yarn material properties.

As a solution, we introduce the compression method as Step 2 to close these artificial gaps in the RVE. To this end, two rigid plates are employed to compress the prepreg RVE in the thickness direction to reduce the thickness to $0.85\ mm$, which is the average value of the real material, see **Fig. 6**. This step is performed using the Abaqus explicit solver and its rationality is supported by the fact that there is no strict constraint for the yarn cross-section shape and the longitudinal path. Fixed boundary conditions are applied to the sides of the RVE to avoid changing its side lengths upon compression. At this stage, the mechanical properties of the prepreg yarn have not be characterized yet because they require calibration by the RVE, whose structure has not been obtained yet. As a result, in the compression simulation, the elastic moduli of the yarn in compression are selected to be the same as the existing ones for the also highly anisotropic cured unidirectional composite. The Poisson's ratios are set to be zero in all directions to avoid altering the yarn width due to the yarn deformation in the thickness direction. It should be noted that these yarn properties are only utilized to generate the RVE structure. They are not the same as the ones in the following sections for the prepreg virtual material characterization. General contact with the hard contact normal behavior is applied to the yarns and the plates to avoid the yarn-to-yarn and yarn-to-plate penetration during the deformation.

After the compression, the corresponding mesh and local material directions of the RVE are exported to evaluate the dimensions and penetration. The yarn thickness is inevitably reduced by around 6% because of the compression, but it is insignificant compared to the 5% variation of the real material value. Apart from the thickness, all other characteristics of this RVE structure are the same as the ones in the real prepreg, and no yarn-to-yarn penetration is observed.

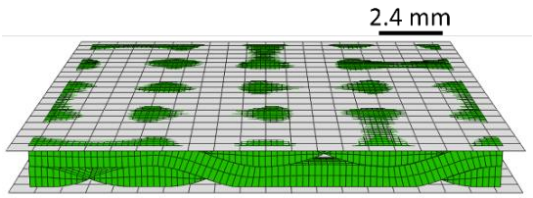

Fig. 6 (Color Online) Prepreg RVE compression in FE software Abaqus: Two rigid plates are introduced to adjust the RVE thickness.

In summary, our 2-step geometrical modeling approach can conveniently generate mesoscopic RVE structure with accurate characteristic dimensions, weave pattern, and yarn packing density of the real material without penetration.

3.2 Mesoscopic Yarn Material Model

In addition to the RVE structure, the yarn material model should also be correctly implemented to have the RVE simulations correspond to reality. Because preforming is a one-step loading process on the uncured prepreg where the material recovery after the deformation is not included, the yarns within the RVE can be assumed to be purely elastic. Furthermore, the prepreg yarns that consist of quasi-unidirectional fibers and uncured resin exbibit a transversely isotropic material property [38]. Direct implementation of such a material behavior, however, leads to numerical errors considering the yarn-yarn interactions and yarn cross-section geometry. We illustrate the possible error with an example where the compression load is applied along the width to a single yarn. This loading condition is quite common for the prepreg in shear deformation where, as

illustrated in **Fig. 7 (a)**, in the real yarn the fibers rearrange as the resin flows. Consequently, the yarn deforms (i.e., its dimensions change) while preserving the basic elliptical shape. In the FE simulation, the yarn is treated as a continuum with relatively flat cross-section geometry where, if the transversely isotropic material model is utilized, numerical errors such as artificial bending and excessive element distortion will appear especially on the edges, as can be seen in **Fig. 7 (b)**. To address this issue, the transverse shear and tension/compression behaviors in the yarn material model are decoupled to control the bending and distortion of the yarn while maintaining its compression property [39, 40]. With this approach, a deformation mode similar to the real material can be achieved, as shown in **Fig. 7 (c)**.

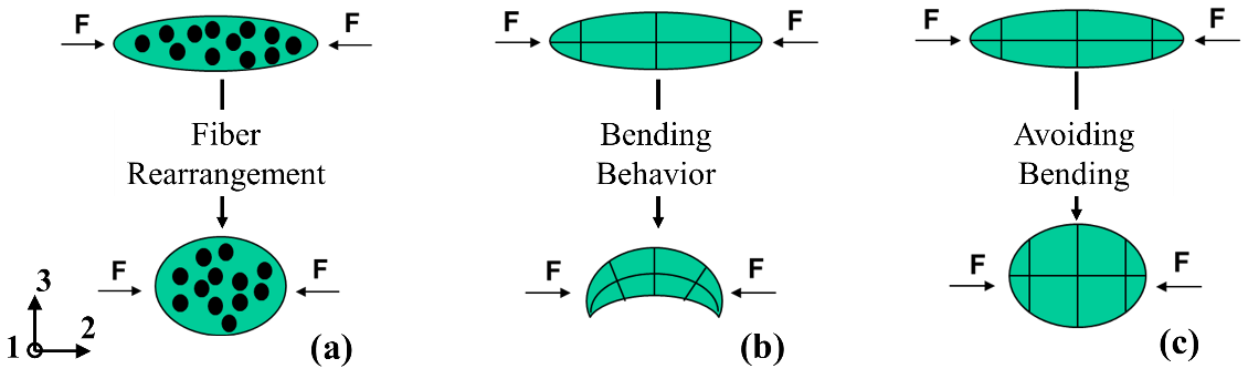

Fig. 7 (Color Online) Illustration of the yarn cross-section deformation upon compression along the width direction: (a) Real material deformation mode, **(b)** FE deformation mode with transversely isotropic material model, and **(c)** FE deformation mode with decoupled material model in FE.

Based on the decoupling approach, we model the yarn using an anisotropic elastic constitutive law with distinct Young's and shear moduli in different directions. This constitutive law is defined in the co-rotational frame which is updated with the deformation gradient tensor to accurately trace the local fiber orientation upon large yarn deformation and rotation under the RVE deformation. In the prepreg yarns, the very stiff carbon fibers are aligned in the longitudinal direction along

which the applied load is predominantly present. Meanwhile, the soft uncured resin governs the transverse deformation. Therefore, it is straightforward to decouple the yarn deformation in the longitudinal and transverse directions by setting both Poisson's ratios ν_{12} and ν_{13} to 0. Additionally, to ensure numerical stability, we set the transverse Poisson's ratio (i.e., ν_{23}) to 0.3. For the yarn shear moduli G_{12}, G_{13} and G_{23}, we coupled them with the transverse modulus of the yarn E_2 for the ease of calibration and manually adjust them to be from 1 to 25 times larger than E_2. It was found that if the shear moduli are too small compared to E_2, the artificial bending in **Fig. 7 (b)** will happen. If they are too large, on the other hand, then significant transverse compression of the yarn will be observed even before the yarn-to-yarn contact. G_{12} and G_{13} to be 15 times larger, and G_{23} to be 10 times larger than E_2 are found to be able to obtain the similar yarn deformation pattern as that observed experimentally. The unknow material properties then are yarn longitudinal modulus E_1, transverse modulus E_2, and friction coefficient μ. The yarn constitutive law is expressed as:

$$d\boldsymbol{\sigma} = \left[S_{ij}\right]^{-1} \cdot d\boldsymbol{\varepsilon} = \begin{bmatrix} \frac{1}{E_1} & 0 & 0 & & & \\ 0 & \frac{1}{E_2} & -\frac{0.3}{E_2} & & \mathbf{0} & \\ 0 & -\frac{0.3}{E_2} & \frac{1}{E_2} & & & \\ & & & \frac{10}{E_2} & 0 & 0 \\ & \mathbf{0} & & 0 & \frac{15}{E_2} & 0 \\ & & & 0 & 0 & \frac{15}{E_2} \end{bmatrix}^{-1} \cdot d\boldsymbol{\varepsilon}, \qquad Eq.3-1$$

where $\boldsymbol{\sigma}$ is the yarn local stress, $\left[S_{ij}\right]$ is the compliance tensor, and $\boldsymbol{\varepsilon}$ is the yarn local strain. Once the structure and the material model of the RVE are generated, they are inputted to the Abaqus

Explicit for FE simulation given the normal true strain along the yarns, the shear angle, and the mesoscopic yarn properties. The normal true strain and the shear are applied via the periodic boundary condition (PBC) to ensure the accurate representation of the deformation by RVE [41]. C3D6 and C3D8 full integration elements are employed for discretization to avoid the hourglass issue. After the simulation, the stress of each element is extracted and averaged to obtain the stress response of the RVE. The mechanical properties of the mesoscopic uncured prepreg yarn including elastic moduli, Poisson's ratios, and friction coefficient are difficult to directly characterize because of the small size, the single yarn specimen preparation, and the soft resin. As a result, we manually adjust the unknow material properties at this stage and the stress prediction from the RVE is compared to the experimental data. One of the best example comparisons is illustrated in **Fig. 8** when E_1, E_2, and μ are 40 GPa, 15 MPa, and 1.0, respectively. The RVE simulation agrees very well with the experiment result when the shear angle is less than 0.6 radian, validating the 2-step approach developed. When the shear angle further increases, the discrepancy between the simulation and the experiment becomes large, indicating the necessities for a proper calibration algorithm, which will be elaborated on in Sec. 4.

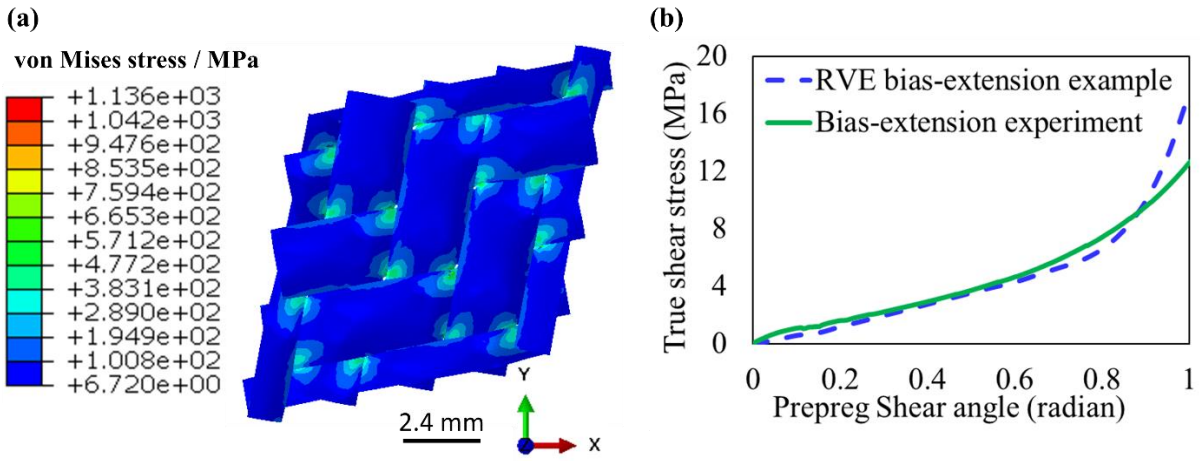

Fig. 8 One bias-extension simulation example using the RVE with $E_1 = 40\ GPa$, $E_2 = 15\ MPa$, and $\mu = 1.0$: (a) Illustration of the von Mises stress contour on the RVE; (b) Comparison of the simulation and experiment true shear stress.

4 Bayesian Calibration of Yarn Material Properties

In this section, we employ experimental data to (i) Estimate the calibration parameters of our RVE simulator (i.e., E_1, E_2, and μ), (i) Determine whether the RVE simulator is biased, and (iii) Build a cheap-to-evaluate emulator to replace the expensive RVE simulator during macroscale analyses. To this end, we adopt a modularized version of the Bayesian calibration framework of Kennedy and O'Hagan (KOH) [42-44]. The Bayesian model updating formulation of KOH is:

$$z(\boldsymbol{x}) = \eta(\boldsymbol{x}, \boldsymbol{\theta}^*) + \delta(\boldsymbol{x}) + \epsilon, \qquad Eq. 4-1$$

where $z(\boldsymbol{x})$ is the true response (which corresponds to experimentally measured stresses in our case), $\boldsymbol{x} = [\varepsilon'_{11}, \varepsilon'_{22}, \gamma'_{12}]^T$ are the controllable inputs, $\boldsymbol{\theta}^* = [E_1^*, E_2^*, \mu^*]^T$ are the true but unknown mesoscopic yarn properties (i.e., the calibration parameters) that do not depend on $\boldsymbol{x}$, $\eta(\boldsymbol{x}, \boldsymbol{\theta})$ is the computer simulator, $\delta(\boldsymbol{x})$ is the bias function, and ϵ is the zero-mean Gaussian noise with unknown variance. ε'_{11}, ε'_{22} denote the normal true strain along the warp and weft yarns, and γ'_{12} represents the shear angle of the fabric. It is noted that we have distinguished between the

generic[1] values of $\boldsymbol{\theta}$ and their true (but unknown) values that correspond to our specific material by placing superscripts on the latter ones. The motivation behind including $\delta(\boldsymbol{x})$ in $Eq. 4-1$ is that no computer simulator is a perfect representation of the corresponding physical system due to, e.g., our lack of knowledge, simplifying or incorrect assumptions, and approximations made to address computational costs.

The goal of Bayesian calibration is to combine three data sources (experiments, simulations, and our prior knowledge) to estimate the unknowns. As illustrated in **Fig. 9**, this process starts by replacing the expensive mesoscopic RVE simulator with the GP emulator (aka metamodel) $\eta(\boldsymbol{x}, \boldsymbol{\theta})$. Then, the uniaxial tension experimental data and the prior knowledge on the mesoscopic yarn properties $p(\boldsymbol{\theta})$ are used to fit the GP emulator $\delta(\boldsymbol{x})$ to the bias function. Our reason for introducing $\delta(\boldsymbol{x})$ is that even if the true calibration parameters were known (which are not) and used in simulations, the stress predictions from the RVE simulator might not match with the experiments. At the third stage, the joint posterior distribution of the mesoscopic yarn properties $p(\boldsymbol{\theta}|\boldsymbol{d})$ are obtained given $\boldsymbol{d}$, i.e., the collection of experimental and simulation data. Finally, the updated emulator is compared against the bias-extension experimental data for validation. Once validated, the updated emulator is used as the constitutive law to predict the stress response of the RVE under any strain state. In the following subsections, we elaborate on each module and provide an extensive tutorial on GP emulation for interested readers in the supporting materials.

We refer the interested readers to [45-48] for detailed discussions on Bayesian updating of computer simulators but note here that the adopted Bayesian formulation: (i) quantifies the uncertainty in the estimated calibration parameters by finding their joint posterior distribution

[1] In a computer simulation, one can choose almost any values for E_1, E_2, and μ.

rather than just a point estimate, and (ii) accounts for prior information and various sources of uncertainty including noise, lack of knowledge such as simulator biases, and data scarcity associated with both experiments and computer simulations.

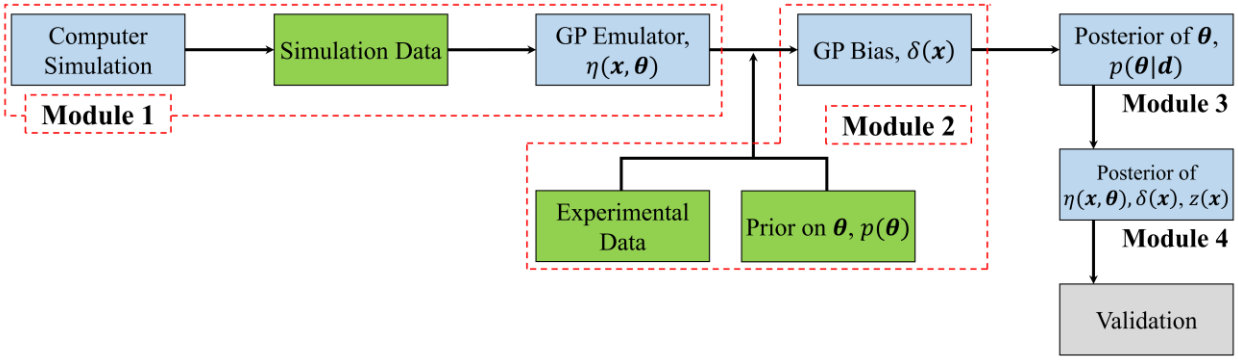

Fig. 9 (Color Online) Modular Bayesian calibration: The approach has four stages and enables estimating the potential simulator bias as well as the joint posterior distribution of the calibration parameters.

4.1 Module 1: GP Modeling of Mesoscopic RVE Simulator

The mesoscopic RVE simulator is computationally expensive, rendering Bayesian calibration (where the stress needs to be evaluated for many combinations of $\boldsymbol{x}$ and $\boldsymbol{\theta}$) infeasible. For instance, the simulation illustrated in **Fig. 8** took 2 hours on 6 12-core Xeon processors. To address this issue, we replace the simulator with the GP emulator $\eta(\boldsymbol{x},\boldsymbol{\theta})$ where $\boldsymbol{x} = [\varepsilon'_{11}, \varepsilon'_{22}, \gamma'_{12}]^T$ and $\boldsymbol{\theta} = [E_1, E_2, \mu]^T$ are defined as before. Once $\eta(\boldsymbol{x},\boldsymbol{\theta})$ is fitted, it can be used for fast prediction of the homogenized mesoscopic stress components $\boldsymbol{\sigma} = [\sigma_{11}, \sigma_{22}, \sigma_{12}]$ for arbitrary combinations of $\boldsymbol{x}$ and $\boldsymbol{\theta}$.

To fit $\eta(\boldsymbol{x},\boldsymbol{\theta})$, we design 200 space-filling experiments with Sobol sequence [49] in the six-dimensional space of $[\boldsymbol{x},\boldsymbol{\theta}]$ with the input ranges of $\varepsilon'_{11} \in [-2,2]\%$, $\varepsilon'_{22} \in [-2,2]\%$, $\gamma'_{12} \in [0,1]\,radian$, $E_1 \in [20,60]\,GPa$, $E_2 \in [5,25]\,MPa$, and $\mu \in [0.15,3]$. The ranges for $\boldsymbol{\theta}$ are chosen wide enough to ensure that the true (but unknown) calibration parameters are covered. The

ranges for $\boldsymbol{x}$ are also selected wide enough to cover the stress values that will be experienced during double-dome preforming simulation in Sec. 5 where $\eta(\boldsymbol{x}, \boldsymbol{\theta})$ will be used as a constitutive law. In each simulation, the material properties are set as $\boldsymbol{\theta}_i$ $(i = 1, \dots, 200)$ while $\boldsymbol{x}_i$ is applied as PBCs. To apply the deformation, the normal true strain along the warp and weft yarns ε'_{11} and ε'_{22} are first applied and then the RVE is sheared to conform to the target shear angle γ'_{12}.

4.2 Module 2: Priors on the Bias Function and Calibration Parameters

In this module, the experimental data and the priors on $\delta(\boldsymbol{x})$ and $\boldsymbol{\theta}$ are used to estimate the parameters of the bias function and the noise variance by maximizing the likelihood that the experimental data follow the formulation in $Eq. 4-1$ [42, 45, 47, 48, 50].

Our experimental data consist of stress-strain curves at 23 °C from the uniaxial tension and bias-extension tests [51], see **Fig. 11**. We hold out the bias-extension data for validation and use 20 equally-spaced data points from the uniaxial tension experiment for calibration. The reasons for using 20 data points rather than the entire curve are that (i) Computational errors and expenses rapidly increase in Bayesian analyses as the dataset size increases, and (ii) 20 points sufficiently characterize the curve in **Fig. 11(c)**: The stable tensile stage contains information on E_1 while the initial undulation stage (which is significantly influenced by the yarn interactions) embodies information on E_2 and μ.

It should be noted that the stress from the RVE simulation is expressed in the orthogonal coordinate which is aligned with the initial yarn directions. The stress from the bias-extension test, however, is expressed in the coordinate that aligns 45 ° from the initial yarn directions. To account for the coordinate transformation, the summation of three stress components from the RVE simulation, i.e., $\frac{(\sigma_{11}+\sigma_{22})}{2} + \sigma_{12}$, is calculated and compared with the stress from the experiment.

Due to the symmetry between σ_{11} and σ_{22} in the bias-extension test, the summation can be simplified to $\sigma_{11} + \sigma_{12}$.

We place a GP prior on the bias function which essentially implies that the posterior of $\delta(\boldsymbol{x})$ is also a GP. GP priors have been successfully used as priors in a wide range of applications to model the potential biases of computer simulators [42, 45, 52-56]. Additionally, as listed in column one in **Table 2**, we choose uniform prior distributions for $\boldsymbol{\theta}$ which cover the entire range where $\eta(\boldsymbol{x}, \boldsymbol{\theta})$ is fitted over. This choice ensures that large variances are used to avoid diminishing the effect of the experimental data on the joint posterior distribution of $\boldsymbol{\theta}$.

Table 2. Prior and posterior distribution of the calibration parameters: The priors on $\boldsymbol{\theta} = [E_1, E_2, \mu]$ are uniform and denoted with $Uni(lower\ bound, upper\ bound)$. Unlike the prior, the posterior distributions of the calibration parameters are neither uniform nor independent.

Prior Distribution	Posterior Mode
$E_1 \sim Uni(20, 60) GPa$, $E_2 \sim Uni(5, 25) MPa$, $\mu \sim Uni(0.15, 3)$	$\begin{bmatrix} 46.8\ GPa \\ 23.5\ MPa \\ 1.3 \end{bmatrix}$

4.3 Module 3: Posterior of the Calibration Parameters

Following **Fig. 9**, the posterior distribution of $\boldsymbol{\theta}$ is obtained via Bayes' theorem after the two GP metamodels $\eta(\boldsymbol{x}, \boldsymbol{\theta})$ and $\delta(\boldsymbol{x})$ are fitted and the noise variance is estimated:

$$p(\boldsymbol{\theta}|\boldsymbol{d}) = \alpha \times p(\boldsymbol{d}|\boldsymbol{\theta}) p(\boldsymbol{\theta}), \qquad Eq. 4-2$$

where $\boldsymbol{d}$ represents the vector of all the available data from both simulations and experiments, $p(\boldsymbol{\theta}|\boldsymbol{d})$ is the posterior of the calibration parameters, $p(\boldsymbol{d}|\boldsymbol{\theta})$ is the Gaussian likelihood, $p(\boldsymbol{\theta})$ is the prior, and α is the normalizing constant that ensures $p(\boldsymbol{\theta}|\boldsymbol{d})$ integrates to 1.

Summary statistics of the posterior distribution are provided in **Table 2**. To obtain more insight into the posterior distributions, the marginal distribution of each parameter is calculated by integrating out the rest of the parameters from the posterior distribution:

$$p(\theta_i|\boldsymbol{d}) = \int_{\boldsymbol{\theta}_{\sim i}} \alpha \times p(\boldsymbol{d}|\boldsymbol{\theta}) p(\boldsymbol{\theta})\, d\boldsymbol{\theta}_{\sim i} \qquad Eq. 4-3$$

where $\boldsymbol{\theta}_{\sim i}$ denotes $\boldsymbol{\theta}$ without the i^{th} element. The results are shown in **Fig. 10** and demonstrate that the marginal variances are relatively large which was expected since (i) there are multiple sources of uncertainty such as experimental and simulation errors and simulator bias, and (ii) limited data are employed in the Bayesian analysis: the calibration data as shown by the dashed black line in **Fig. 11(a)** is only available on a three dimensional (3D) curve in the 3D strain space. It should be noted here that the upper bound on E_1 is smaller than the homogeneous longitudinal Young's modulus of general cured carbon fiber composite yarns with 50% fiber volume fraction (i.e., 110 GPa) because (i) the fiber volume fraction in the uncured prepreg is smaller than that in the cured prepreg since the resin flows out under pressure in curing, and (ii) the fabric in the uncured prepreg is loose, i.e., the fiber have local waviness which reduces the yarn's longitudinal modulus under tension. Research work in [57] shows a similar uncured prepreg yarn's longitudinal modulus of around 46.4 GPa.

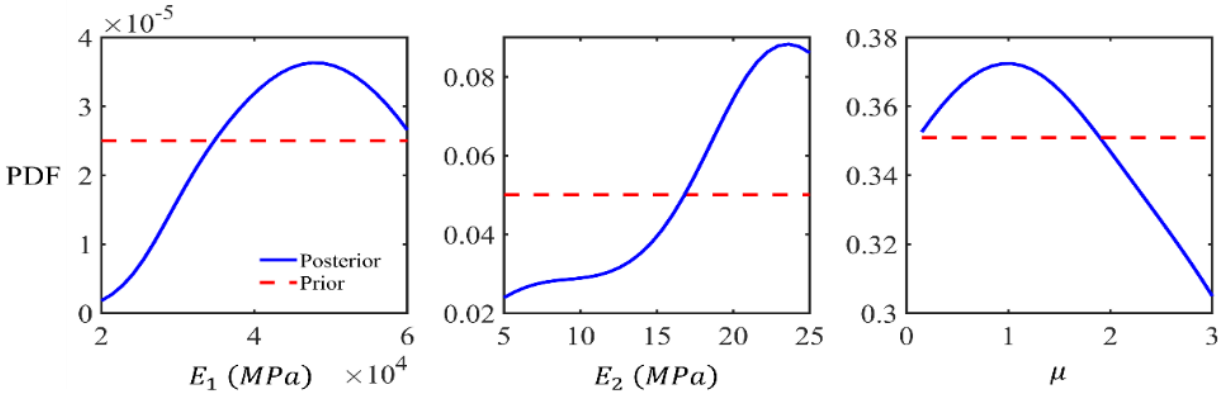

Fig. 10 (Color Online) Marginal posterior distributions on the calibration parameters: The posterior and prior are indicated with solid blue and dotted red lines, respectively.

4.4 Module 4: Posterior of the Responses

To predict the stress for an arbitrary deformation state, $Eq.4-1$ can be employed. However, since $\boldsymbol{\theta}^*$ is not known, $\boldsymbol{\theta}$ is used in the right-hand side (RHS) of $Eq.4-1$. To eliminate the dependency of the RHS on $\boldsymbol{\theta}$, the RHS is then integrated with respect to the posterior distribution of $\boldsymbol{\theta}$. This integration is generally done via, e.g., Monte Carlo methods and quadrature rules. In this work, we use quasi Monte Carlo.

Fig. 11 illustrates the predictions of the orthogonal stress components by the updated emulator under various deformation states. The normal stress σ_{11} is plotted against the normal true strain along warp and weft yarns, ε'_{11} and ε'_{22}, for two different values of γ'_{12} in **Fig. 11 (a)**. Similarly, the shear stress σ_{12} is plotted in **Fig. 11 (b)** where its symmetry with respect to ε'_{11} and ε'_{22} is evident. Compared to σ_{12}, σ_{11} is less sensitive to γ'_{12}. It can also be observed that σ_{12} monotonically increases as any of the strain components increase. This monotonic behavior is also observed in **Fig. 11 (a)** but is slightly compromised when there is no shear strain (i.e., in the red surface). This small inconsistency may be due to (i) numerical issues such as the high strain rate

to reduce the run-time in the RVE simulation, and (ii) lack of simulation data with very small γ'_{12} which results in extrapolation during the Bayesian calibration.

In **Fig. 11 (c)** the uniaxial tension test is plotted. Since this test was used for calibration, the model predictions are expected to match the test data. In **Fig. 11 (d)** the bias extension test and our predictions are plotted. Since this data are not used in calibration, this figure illustrates that the calibration has been effective in learning the stress-strain behavior. The posterior of the resulting GP model (i.e., the left-hand-side in $Eq.4-1$) can now be used as the constitutive law of integration points in the macroscopic preforming simulations.

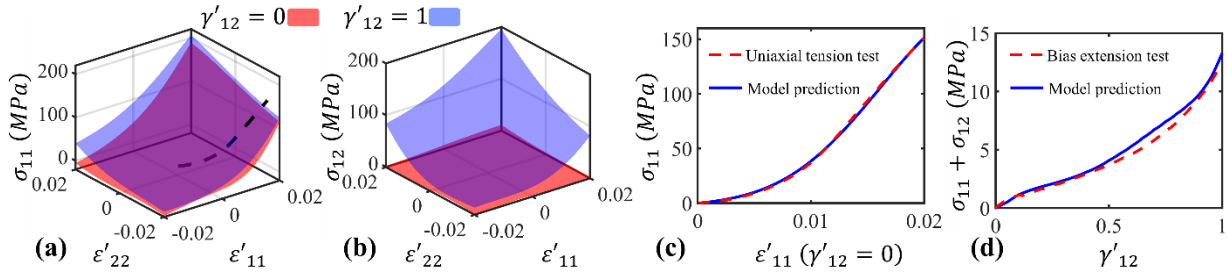

Fig. 11 (Color Online) Posterior mean of the responses: (a) Normal stress as a function of normal true strain along the yarns for two different shear angles. **(b)** Shear stress as a function of normal true strain along the yarns for two different fabric shear angle. **(c)** Uniaxial tension test used in calibration vs. our predictions. **(d)** Bias extension test which is not used in calibration vs. our predictions.

To demonstrate the effect of including the bias function in $Eq.4-1$, we illustrate its posterior distribution in **Fig. 12** under the two experimental setup conditions. In the uniaxial tension test, the posterior of $\delta(\boldsymbol{x})$ is positive, indicating that the stress predictions from the RVE simulator are generally smaller (around 10%, compare the y-axis of **Fig. 11(c)** and **Fig. 12(a)**) than the experimentally measured stresses. The slight curvature in **Fig. 12(a)** is mainly due to numerical errors and noise. In the bias extension test, the posterior of $\delta(\boldsymbol{x})$ is initially positive and then negative. This implies that our RVE simulator first underestimates the stress and then

overestimates it. The underestimation is due to neglecting the large static friction coefficient (due to the large relative sliding/rotation between the prepreg yarns during preforming) and only including the dynamic coefficient in the RVE. The reason behind overestimation is that in the real specimen, when the shear deformation is very large and closed to shear locking, there might be some slight sliding and "pull-out" of yarns to reduce the pure shear resistance. This deformation mode is not measured during the experiment and is neglected in the RVE as it only happens near the shear locking. As a result, the RVE model will overestimate the stress prediction when the shear deformation is large.

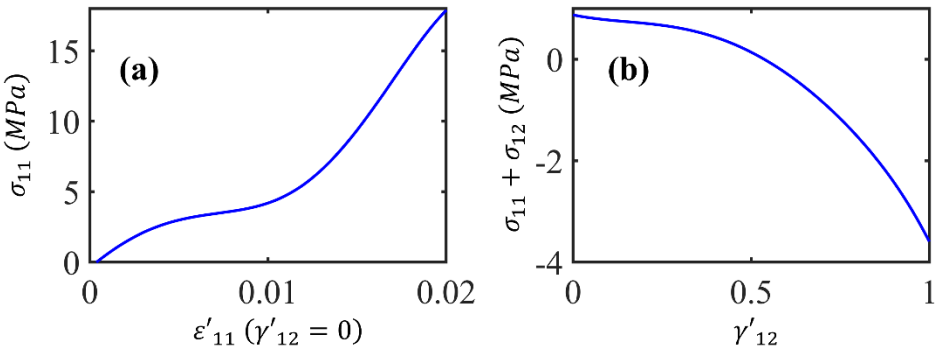

Fig. 12 (Color Online) Posterior of the bias function: The posterior is obtained under two loading conditions **(a)** uniaxial tension, and **(b)** bias extension.

5 Integration of the Mesoscopic Emulator with Macroscopic Preforming Simulation

As the constitutive law of the 2x2 twill prepreg with uncured thermoset resin, the mesoscopic stress emulator obtained in Sec. 4, is implemented into Abaqus Explicit in the non-orthogonal coordinate [14] as VUMAT for the macroscopic preforming process simulation. For this multiscale constitutive law, the deformation input consists of the normal true strain ε'_{11} and ε'_{22} along the warp and the weft yarn directions, and the shear angle γ'_{12}. These inputs are all calculated using

the non-orthogonal coordinate algorithm. The predicted stress components $\boldsymbol{\sigma} = [\sigma_{11}, \sigma_{22}, \sigma_{12}]$ are obtained in the Abaqus orthogonal material coordinate directly. Hence, the constitutive law does not require coordinate transformation of the stress and has the following format:

$$\begin{bmatrix}\sigma_{11}\\ \sigma_{22}\\ \sigma_{12}\end{bmatrix} = \begin{bmatrix}\sigma_{11}\left(\varepsilon'_{11}, \varepsilon'_{22}, \gamma'_{12}\right)\\ \sigma_{22}\left(\varepsilon'_{11}, \varepsilon'_{22}, \gamma'_{12}\right)\\ \sigma_{12}\left(\varepsilon'_{11}, \varepsilon'_{22}, \gamma'_{12}\right)\end{bmatrix}, \qquad Eq. 6-1$$

We note that our emulator is learned over the range of $\varepsilon'_{11} \in [-2, 2]\%$, $\varepsilon'_{22} \in [-2, 2]\%$, $\gamma'_{12} \in [0, 1]\ radian$. Both tensile and compressive behaviors are considered in the emulator. This emulator is applied to each of the five individual integration points in the through-the-thickness direction of the S4R shell element, and therefore, the bending behavior of the prepreg is captured in the preforming simulation. For the deformation states outside these ranges, the prepreg will transfer into the shear locking state, and the VUMAT employs the shear locking state algorithm from the decoupled non-orthogonal model [14].

The macroscopic double-dome benchmark preforming experiment is simulated with the multiscale VUMAT for the prepreg with uncured thermoset resin at 23 °C. The simulation setup is illustrated **Fig. 13 (a)**: One layer of prepreg in ±45 fiber orientation is formed in this process where the displacement of the punch is 90 mm, and the binder force increases linearly from 4000 N to 8200 N based on the experimental measurements. The thickness of the prepreg layer is orders of magnitude smaller compared to its length and width, so the prepreg is discretized by S4R shell elements to reduce the computational cost. The tools are simulated as rigid bodies, hence, their element type will not affect the simulation results. S3 elements are selected to discretize the tools because of their excellent auto-mesh capability for complex geometries. The friction coefficient

between the tool and the prepreg is set to 0.3 according to the experimental measurement. This friction coefficient, as well as the one between the yarn in the mesoscopic RVE, is the constant dynamic one. The reason is that the preforming process leads to large prepreg deformation which, in turn, results in large sliding between the tools and prepreg at the macroscale and large sliding and rotation between the yarns at the mesoscale. Hence, the static friction is neglected.

The simulation result is compared against the one obtained from the tension-shear decoupled non-orthogonal material model developed in [14] which is also calibrated via the same experimental data. The final prepreg sheet geometry and the yarn angle distribution results are demonstrated in **Fig. 13 (b)** together with the real preformed part. The draw-in distance and the yarn angle at the sampling locations from the simulation and the experiment are listed in **Table 3**. The comparison indicates that our method with the tension-shear coupling effect leads to a slight improvement for the draw-in and yarn angle at locations A to F over the decoupled model.

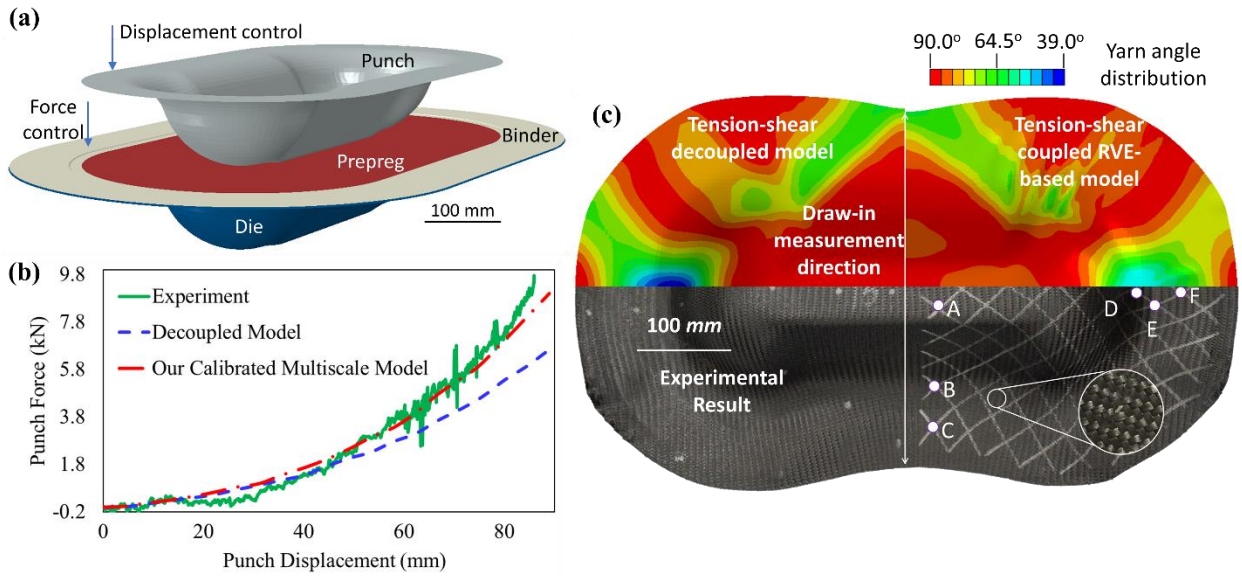

Fig. 13 (Color online) Preforming simulation: (a) Simulation setup, **(b)** Final part shapes and yarn angle distributions, and (c) Punch force comparison. In **(b)**, the A-E points indicate the yarn angle measuring positions.

The punch force-displacement curves from the two simulation cases and the experiment are compared in **Fig. 13 (c)**. The plots demonstrate that the new multiscale preforming simulation method predicts the punch force with much higher accuracy compared to the simulation using the decoupled material model. The small discrepancy between the forces from the new simulation method and the experiment when the punch displacement reaches to over $70\ mm$ may be caused by the negligence of the prepreg thickness variation by the shell elements in the simulation. The small force discrepancy when the punch displacement ranges from 20 to $50\ mm$, however, may be resulted from the fact that the temperature at some locations of the prepreg has not reached to 23 ℃ completed at the initial stage of the preforming, leading to softer material behavior compared to the one for the simulation.

Table 3. Draw-in distance and yarn angle comparison between the simulation and the experiment: The simulation results are from the new multiscale material model and the tension-shear decoupled material model.

Comparison	Draw-in	A	B	C	D	E	F
Multiscale model	$42.25\ mm$	86°	88°	73°	54°	57°	67°
Decoupled model	$40.22\ mm$	89°	89°	71°	40°	45°	65°
Experiment	$49.02\ mm$	80°	88°	71°	49°	56°	66°

As a summary, our newly developed Bayesian calibrated material model with tension-shear coupling for multiscale simulation of prepreg preforming can predict the draw-in distance and the yarn angle variation on the preformed prepreg. More importantly, it also predicts the punch force history with high accuracy. This new multiscale model, therefore, has stronger predictive capability and can serve as a powerful tool for part performance prediction, process parameters optimization, material design, and defect analysis for future preforming works.

6 Conclusion and Future Work

In this paper, we developed a numerical Bayesian-calibrated characterization method for identifying material behavior of a prepreg in preforming based on a new multiscale material model consisting of the mesoscopic RVE and the macroscopic process simulation. This method can take the tension-shear coupling effect into consideration, which is important for accurately predicting preforming force and the resulting blank shape. In our approach, a new 2-step FE modeling technique is first developed to generate the mesoscopic prepreg RVE structure. This RVE is then utilized to identify the complex tension-shear coupling effect of the woven prepreg at the condition of the preforming. The Bayesian calibration is applied to the RVE simulator to identify the mesoscopic yarn material properties, which are difficult to be directly measured via physical tests. The calibration algorithm also provides an inexpensive but accurate GP emulator which replaces the computationally costly mesoscopic RVE simulator that is used at each integration point in the macroscopic preforming simulation. For the multiscale part, the mesoscopic stress emulator is implemented into Abaqus Explicit in the non-orthogonal coordinate as VUMAT so that the tension-shear coupling effect of the woven prepreg can be considered in the mesoscopic preforming simulation. The comparison for preforming a double-dome geometry used in the benchmark test [28] between the simulation with the new multiscale material model, the tension-shear decoupled non-orthogonal model, and the experimental result indicates that our new model is superior to the decoupled one and can reliably predict draw-in distance, yarn angle distribution, and punch force in the preforming process.

We calibrated the GP stress emulator via the uniaxial tension test and validated it against the bias-extension test. Employing other tests with different loading conditions such as biaxial tension will provide additional evidence of the model validity. Additionally, we used material properties

at constant temperatures while this is not the case in the experiments where the cooling effect from tools and air affects prepreg mechanical behaviors. Considering temperature-dependent properties to achieve a higher accuracy is recommended for future work. Moreover, the multiscale method presented here is established in a hierarchical scheme, so the path dependency of the prepreg deformation is neglected. The concurrent scheme can be utilized in future work for the multiscale preforming simulation to model the prepreg behavior with higher fidelity.

Acknowledgments

This work is supported by a subcontract from the Ford Motor Company with funding from the Office of Energy Efficiency and Renewable Energy (EERE), U.S. Department of Energy, under Award Number DE-EE0006867.

7 References

1. Wang, M., Q. Kang, and N. Pan, *Thermal conductivity enhancement of carbon fiber composites.* Applied Thermal Engineering, 2009. **29**(2): p. 418-421.
2. Che, D.M., et al., *Machining of Carbon Fiber Reinforced Plastics/Polymers: A Literature Review.* Journal of Manufacturing Science and Engineering-Transactions of the Asme, 2014. **136**(3): p. 034001-1-034001-22.
3. Das, S., *Life cycle assessment of carbon fiber-reinforced polymer composites.* The International Journal of Life Cycle Assessment, 2011. **16**(3): p. 268-282.
4. Jauffrès, D., et al., *Discrete mesoscopic modeling for the simulation of woven-fabric reinforcement forming.* International Journal of Material Forming, 2010. **3**(2): p. 1205-1216.
5. Baker, D.A. and T.G. Rials, *Recent advances in low-cost carbon fiber manufacture from lignin.* Journal of Applied Polymer Science, 2013. **130**(2): p. 713-728.
6. Bostanabad, R., et al., *Stochastic microstructure characterization and reconstruction via supervised learning.* Acta Materialia, 2016. **103**: p. 89-102.
7. Young, W.-B. and C.-W. Tseng, *Study on the pre-heated temperatures and injection pressures of the RTM process.* Journal of Reinforced Plastics and Composites, 1994. **13**(5): p. 467-482.
8. Rosenberg, P., et al., *Investigating cavity pressure behavior in high-pressure RTM process variants.* AIP Conference Proceedings, 2014. **1593**(1): p. 463-466.
9. Sloan, J., *ATL & AFP: Defining the megatrends in composite aerostructures.* High performance composites, 2008. **16**(4): p. 68.

10. Grimshaw, M.N., C.G. Grant, and J.M.L. Diaz. *Advanced technology tape laying for affordable manufacturing of large composite structures*. in *International sampe symposium and exhibition*. 2001. SAMPE; 1999.
11. Lukaszewicz, D.H.J.A., C. Ward, and K.D. Potter, *The engineering aspects of automated prepreg layup: History, present and future.* Composites Part B: Engineering, 2012. **43**(3): p. 997-1009.
12. Marsh, G., *Automating aerospace composites production with fibre placement.* Reinforced Plastics, 2011. **55**(3): p. 32-37.
13. Suratno, B.R., L. Ye, and Y.-W. Mai, *Simulation of temperature and curing profiles in pultruded composite rods.* Composites Science and Technology, 1998. **58**(2): p. 191-197.
14. Zhang, W., et al., *A non-orthogonal material model of woven composites in the preforming process.* CIRP Annals, 2017. **66**(1): p. 257-260.
15. Wulfsberg, J., et al., *Combination of Carbon Fibre Sheet Moulding Compound and Prepreg Compression Moulding in Aerospace Industry.* Procedia Engineering, 2014. **81**(Supplement C): p. 1601-1607.
16. Hsiao, S.-W. and N. Kikuchi, *Numerical analysis and optimal design of composite thermoforming process.* Computer Methods in Applied Mechanics and Engineering, 1999. **177**(1): p. 1-34.
17. Zhang, W., et al., *An integrated computational materials engineering method for woven carbon fiber composites preforming process.* AIP Conference Proceedings, 2016. **1769**(1): p. 170036.
18. Botelho, E.C., et al., *Mechanical behavior of carbon fiber reinforced polyamide composites.* Composites Science and Technology, 2003. **63**(13): p. 1843-1855.
19. Bostanabad, R., et al., *Uncertainty quantification in multiscale simulation of woven fiber composites.* Computer Methods in Applied Mechanics and Engineering, 2018. **338**: p. 506-532.
20. Ten Thije, R.H.W., R. Akkerman, and J. Huétink, *Large deformation simulation of anisotropic material using an updated Lagrangian finite element method.* Computer Methods in Applied Mechanics and Engineering, 2007. **196**(33–34): p. 3141-3150.
21. Hamila, N., et al., *A semi-discrete shell finite element for textile composite reinforcement forming simulation.* International Journal for Numerical Methods in Engineering, 2009. **79**(12): p. 1443-1466.
22. Sharma, S.B. and M.P.F. Sutcliffe, *A simplified finite element model for draping of woven material.* Composites Part A: Applied Science and Manufacturing, 2004. **35**(6): p. 637-643.
23. Lee, W. and J. Cao, *Numerical simulations on double-dome forming of woven composites using the coupled non-orthogonal constitutive model.* International Journal of Material Forming, 2009. **2**(1): p. 145.
24. Cao, J., et al., *Characterization of mechanical behavior of woven fabrics: Experimental methods and benchmark results.* Composites Part A: Applied Science and Manufacturing, 2008. **39**(6): p. 1037-1053.
25. Boisse, P., et al., *Simulation of wrinkling during textile composite reinforcement forming. Influence of tensile, in-plane shear and bending stiffnesses.* Composites Science and Technology, 2011. **71**(5): p. 683-692.

26. Launay, J., et al., *Experimental analysis of the influence of tensions on in plane shear behaviour of woven composite reinforcements.* Composites Science and Technology, 2008. **68**(2): p. 506-515.
27. Gereke, T., et al., *Experimental and computational composite textile reinforcement forming: A review.* Composites Part A: Applied Science and Manufacturing, 2013. **46**: p. 1-10.
28. *Woven composites benchmark forum*. 2008; Available from: http://www.wovencomposites.org.
29. Wan, Y., et al., *Predicting dynamic in-plane compressive properties of multi-axial multi-layer warp-knitted composites with a meso-model.* Composites Part B: Engineering, 2015. **77**: p. 278-290.
30. Giannaros, E., et al., *Implementation and calibration of meso-scale modeling technique for simulation of tensile behavior of fabric materials.* Composites Part B: Engineering, 2017. **119**: p. 1-9.
31. Sherburn, M., *Geometric and Mechanical Modelling of Textiles*. 2007.
32. Verpoest, I. and S.V. Lomov, *Virtual textile composites software WiseTex: Integration with micro-mechanical, permeability and structural analysis.* Composites Science and Technology, 2005. **65**(15): p. 2563-2574.
33. Lomov, S.V., et al., *Meso-FE modelling of textile composites: Road map, data flow and algorithms.* Composites Science and Technology, 2007. **67**(9): p. 1870-1891.
34. Hivet, G. and P. Boisse, *Consistent 3D geometrical model of fabric elementary cell. Application to a meshing preprocessor for 3D finite element analysis.* Finite Elements in Analysis and Design, 2005. **42**(1): p. 25-49.
35. Naouar, N., et al., *Meso-scale FE analyses of textile composite reinforcement deformation based on X-ray computed tomography.* Composite Structures, 2014. **116**: p. 165-176.
36. Desplentere, F., et al., *Micro-CT characterization of variability in 3D textile architecture.* Composites Science and Technology, 2005. **65**(13): p. 1920-1930.
37. Khan, A.H. and R.A. Chaudhuri, *Fan-beam geometry based inversion algorithm in computed tomography (CT) for imaging of composite materials.* Composite Structures, 2014. **110**: p. 297-304.
38. Bonet, J. and A.J. Burton, *A simple orthotropic, transversely isotropic hyperelastic constitutive equation for large strain computations.* Computer Methods in Applied Mechanics and Engineering, 1998. **162**(1): p. 151-164.
39. Charmetant, A., E. Vidal-Sallé, and P. Boisse, *Hyperelastic modelling for mesoscopic analyses of composite reinforcements.* Composites Science and Technology, 2011. **71**(14): p. 1623-1631.
40. Wang, D., et al., *Longitudinal compression and Poisson ratio of fiber yarns in meso-scale finite element modeling of composite reinforcements.* Composites Part B: Engineering, 2018. **141**: p. 9-19.
41. Xiaodong, T. and D.W. John, *General Techniques for Exploiting Periodicity and Symmetries in Micromechanics Analysis of Textile Composites.* Journal of Composite Materials, 2003. **37**(13): p. 1167-1189.
42. Kennedy, M.C. and A. O'Hagan, *Bayesian calibration of computer models.* Journal of the Royal Statistical Society: Series B (Statistical Methodology), 2001. **63**(3): p. 425-464.

43. Bostanabad, R., et al., *Leveraging the nugget parameter for efficient Gaussian process modeling.* International Journal for Numerical Methods in Engineering, 2018. **114**(5): p. 501-516.
44. Bostanabad, R., et al., *Computational microstructure characterization and reconstruction: Review of the state-of-the-art techniques.* Progress in Materials Science, 2018. **95**: p. 1-41.
45. Bayarri, M., et al., *Computer model validation with functional output.* The Annals of Statistics, 2007: p. 1874-1906.
46. Conti, S. and A. O'Hagan, *Bayesian emulation of complex multi-output and dynamic computer models.* Journal of statistical planning and inference, 2010. **140**(3): p. 640-651.
47. Arendt, P.D., D.W. Apley, and W. Chen, *Quantification of model uncertainty: Calibration, model discrepancy, and identifiability.* Journal of Mechanical Design, 2012. **134**(10): p. 100908.
48. Arendt, P.D., et al., *Improving identifiability in model calibration using multiple responses.* Journal of Mechanical Design, 2012. **134**(10): p. 100909.
49. Sobol, I.M., *On quasi-Monte Carlo integrations.* Mathematics and Computers in Simulation, 1998. **47**(2-5): p. 103-112.
50. Mansoori, F. and E. Wei, *Superlinearly Convergent Asynchronous Distributed Network Newton Method.* arXiv preprint arXiv:1705.03952, 2017.
51. Zhang, W., et al. *Experimental methods to characterize the woven composite prepreg behavior during the preforming process*. in *31st Annual Technical Conference of the American Society for Composites, ASC 2016*. 2016. DEStech Publications Inc.
52. Higdon, D., et al., *Combining field data and computer simulations for calibration and prediction.* SIAM Journal on Scientific Computing, 2004. **26**(2): p. 448-466.
53. Jenný, B. and O. Anthony, *Learning about physical parameters: the importance of model discrepancy.* Inverse Problems, 2014. **30**(11): p. 114007.
54. Bogdanor, M.J., C. Oskay, and S.B. Clay, *Multiscale modeling of failure in composites under model parameter uncertainty.* Computational Mechanics, 2015. **56**(3): p. 389-404.
55. Joseph, V.R. and H. Yan, *Engineering-driven statistical adjustment and calibration.* Technometrics, 2015. **57**(2): p. 257-267.
56. Arendt, P.D., D.W. Apley, and W. Chen, *A preposterior analysis to predict identifiability in the experimental calibration of computer models.* IIE Transactions, 2016. **48**(1): p. 75-88.
57. Buet-Gautier, K. and P. Boisse, *Experimental analysis and modeling of biaxial mechanical behavior of woven composite reinforcements.* Experimental Mechanics, 2001. **41**(3): p. 260-269.